EXPERIMENTAL RELATIONS BETWEEN STRESS AND FRACTURE PROPERTIES IN SYNTHETIC ANISOTROPIC MEDIA

P.E.P. Marcondes, J.J.S. Figueiredo, M.E. Far, J. Schleicher, N. Dyaur, and R.R. Stewart

email: *paulo.pasquini@petrobras.com.br*

keywords: *Physical modelling, seismic waves, anisotropy, fractures*

ABSTRACT

There is a need in the industry to geometrically and mechanically characterize fractures by means of seismic experiments. To study this problem, we carried out physical-modelling experiments with Plexiglas bodies, simulating fractures with a low-shear-modulus filling by using neoprene rubber discs as inclusions. We carried out pulse transmission measurements of P- and S-wave velocities in a reference model without inclusions and in a model with penny-shaped neoprene inclusions. The background model is an anisotropic matrix that consists of stacked Plexiglas plates. Rubber disc inclusions in that anisotropic matrix leading to secondary anisotropy. We recorded ultrasonic seismic data using P-wave transducers with central frequency 120 kHz and S-wave transducers with 90 kHz. We compressed the physical models using pressures ranging from 3 to 15.8 MPa. Full crack closure occurs at stress 14.6 MPa normal to model faces. Our analysis indicates different regimens for the behaviour of the inclusions when observed via its crack densities and aspect ratios. These results suggest a different dependence of the crack aspect ratio on uniaxial stress at lower stresses than usually described in the literature. Other results point toward the possibility to characterize a fractured medium though its elastic coefficients. Though our results are not extensive, they show that simple experimental approaches can provide valuable insight into the behaviour of cracked rocks at reservoir stress levels.

INTRODUCTION

Fault and fracture characterization is very important for hydrocarbon reservoirs, because these kinds of structures can act as flow barriers or conduits (Aguilera, 1998; Nelson, 2001). In the last three decades, there has been a growing number of papers that deal mathematically the question of wave propagation in media with differing degrees of fracturing. With the aim to better understand faults and fractures geometrically and mechanically, elastic anisotropy due to aligned cracks has been also the subject of many seismic physical modelling experiments. Many advances were only possible due to improvements in seismic acquisition and processing technologies.

However, due to the complexity of seismic wave propagation in fractured anisotropic media, fully characterizing these kind of media is not always possible. Tsvankin (2005) observes that certain types of anisotropy cannot be fully characterized with current seismic technologies. The effective anisotropy of a region could be associated with alternating layers with thickness smaller than a wavelength (Krey and Helbig, 1956; Figueiredo, 2012) or with preferential orientation or the degree of fracturing in the rocks (Crampin, 1981, 1984a,b; Schoenberg and Sayers, 1995; Figueiredo, 2012; Figueiredo et al., 2012b). Under these conditions, the adoption of simplified models and geometries as well as adequate parameter choices permit the reliable characterization of these media in both numerical and physical seismic modelling studies.

As has been pointed out by Figueiredo (2012), numerical modelling needs to employ certain simplifications in the representation of fractured media that can result in numerical dispersion among other issues. In such situations, physical modelling with careful choice of the model's dimensions and constituent materials can serve as a useful link between theoretical developments, numerical models, and field data. In situations when one can count on all four of approaches (theoretical, numerical, physical models and field data), it is possible to evaluate how well seismic wave-propagation phenomena are understood and make a meaningful contribution to the advancement of the body of knowledge in the field.

In this sense, the main objective of this study is to contribute with physical observations to the seismic characterization of faults and fractures. Through simplified models, we attempt at observing the behaviour of inclusions (as proxies to fractures) in a polar anisotropic background. Under external compression simulating reservoir stress, we carried out ultrasonic measurements as described in detail in Figueiredo (2012) and Figueiredo et al. (2012b) on two models representing two geological cases. One is relief jointing, caused by the decompression of rocks, that may be due to uplift or a free surface. The other represents stilolites, i.e., discontinuities generated by pressure dissolution, usually found in carbonate rocks.

The modelling aimed at simulating fractures filled with a low-shear-modulus material. This material would represent clay or fluids, containing or not hydrocarbons. Thus, due to its low shear modulus, we used inclusions made of neoprene rubber. Specifically, the main objective was to describe the medium behaviour in terms of fracture densities and their aspect ratios. Additionally, we wanted to determine the effect of these inclusions on the elastic and anisotropic parameters of a model in which the background was already polar anisotropic.

PHYSICAL MODELLING

Model Building

As previously mentioned, model building and ultrasonic data acquisition were carried out at the Allied Geophysical Laboratories (AGL) of the University of Houston (Figueiredo et al., 2011a,b; Figueiredo, 2012; Figueiredo et al., 2012a,b; Marcondes et al., 2012a,b). The first model is the anisotropic *reference model*, which can be seen in Figure 1a. It consists of 55, 1.5 mm thick Plexiglas plates, perforated at the corners for the addition of an anti-slip device. The plates measured 93.4×95.5 mm $(x \times y)$. The uncompressed stack of 55 plates measured 84.1 mm in height.

54 of these Plexiglas plates were used again for the construction of the model with inclusions (one broke during the experiment with the reference model). In the cracked model, 30 neoprene rubber discs were inserted between each pair of plates. The discs were 3.6 mm in diameter and 0.57 mm thick. In this way, we expected to simulate a set of weakly filled fractures, with orientation parallel to the maximum vertical stress. A measuring tape was embedded below the last plate to allow measuring the inclusion diameter during the experiment (see Figure 1b). After the neoprene discs were added, the vertical model dimension was 84.24 mm before the application of compression, all other dimensions were unchanged. In order to ensure that all discs had the same diameter, a special puncher was used to cut the neoprene inclusions from the rubber sheet. Since the inclusions were distributed uniformly, and since the plates and neoprene discs adhere well, variation in diameter is considered to be uniform for all discs in the model.

Fracture density ε can be estimated according to the formula proposed by Hudson (1981),

$$\varepsilon = \frac{NV_c}{V} = \frac{N\pi r^2 h}{V} \, , \tag{1}$$

where N is the number of fractures, V_c is the volume of a single fracture and V is the volume of the model. For penny shaped inclusions, $V_c = \pi r^2 h$, where r is the radius of the inclusion and h is the thickness of the inclusion.

Ultrasonic Experiment

For the ultrasonic experiment, S-wave transducers were located on opposite sides of the models. Initially the polarisation was parallel to the plates and then rotated in 18 steps of 10 degrees. Polarisations 0 and $180°$ represent fast S-wave (S_1) and those at $90°$ represent slow S-waves(S_2). There is a 2.7 μs delay for the S-wave transducers and 2.9 μs delay for the P-wave transducers. During the experiment, uniaxial stress

was increased in 12 steps, from 3 up to 15.8 MPa using the device conceived by Omoboya et al. (2011). The equipment is depicted in Figure 2 and a schematic representation of the experiment apparatus is shown on Figure 3. Seismic signatures and spectra for both transducers are shown in Figures 4 and 5.

The ultrasonic signal was digitized using a scale factor of 1:10 000, to bring the frequencies into the seismic range. The transducer-induced delay was subtracted from the arrival times during velocity calculations. The arrival picking accuracy is ± 0.2 μs, which yields errors in velocities of the order of ± 4 m/s.
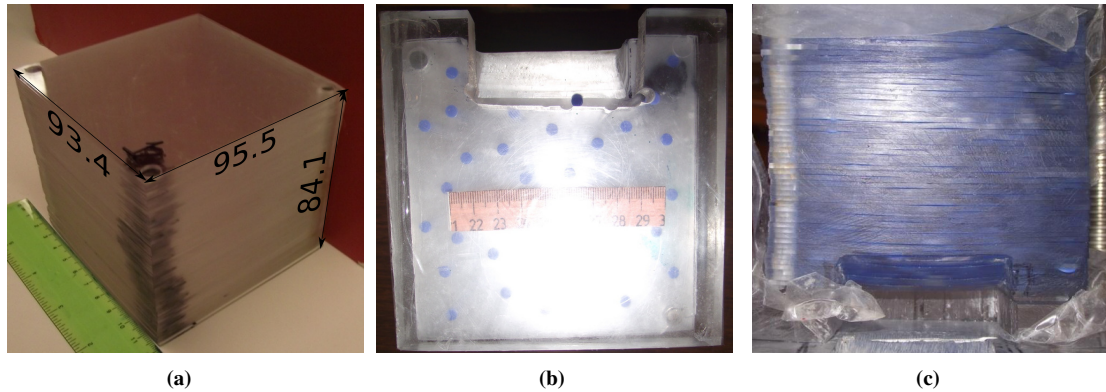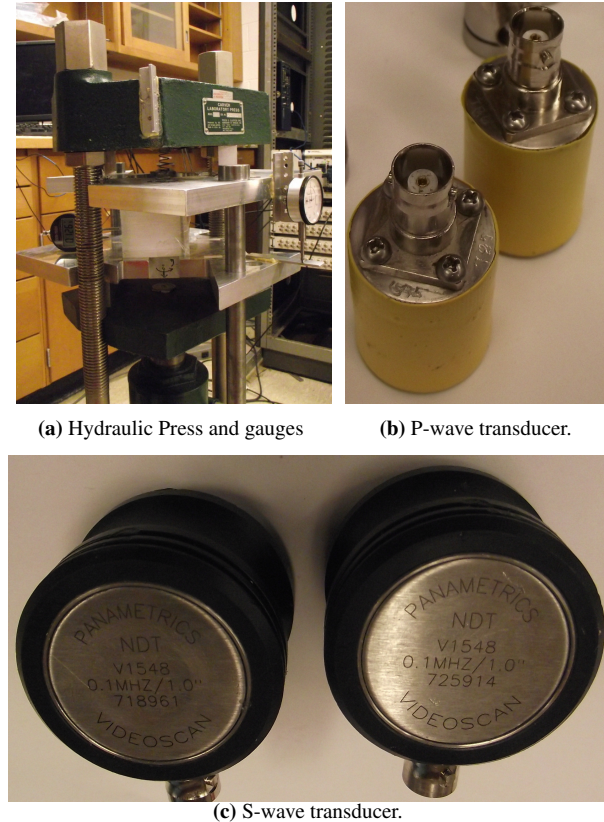

(a) **(b)** **(c)**

Figure 1: Anisotropic models: (a) reference model, 55 stacked Plexiglas plates. (b) Model with inclusions, top view before the experiment. (c) Side view after the experiment.

(a) Hydraulic Press and gauges **(b)** P-wave transducer.

(c) S-wave transducer.

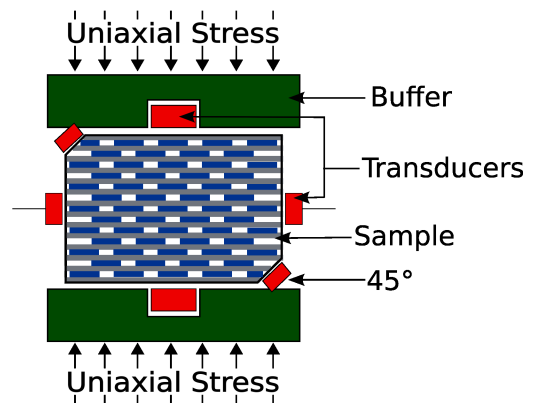**Figure 2:** Equipment used in the experiment.

Figure 3: Schematic positioning of transducers (drawn in red). The Plexiglas plates are shown in gray and the inclusions in blue. In green is the Plexiglas block, the *buffer*.
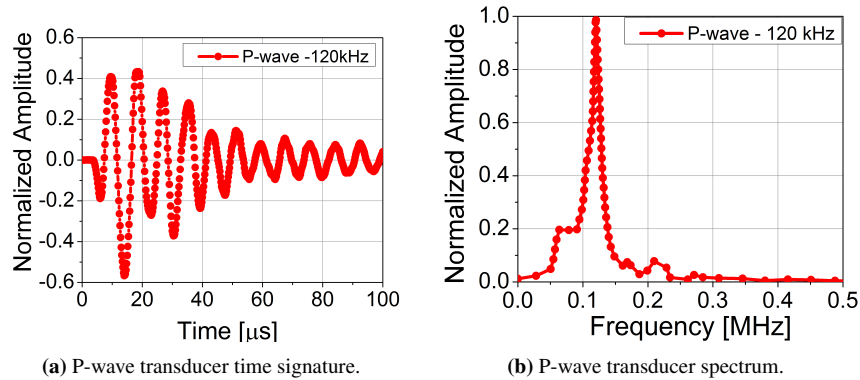
(a) P-wave transducer time signature.

(b) P-wave transducer spectrum.

Figure 4: Spectrum and signature of the P-wave transducer.

(a) S-wave transducer time signature
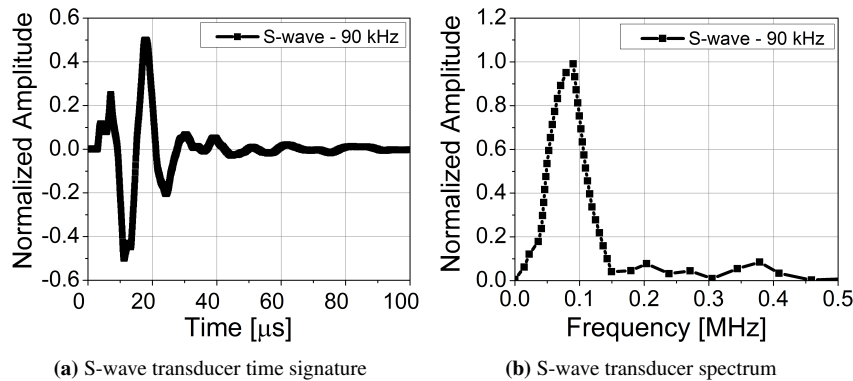
(b) S-wave transducer spectrum

Figure 5: Spectrum and time signature of S-wave transducer used in this study.

Quality Control

Besides determining the P, S_1, and S_2 wave velocities in the models, we also measured these velocities in the Plexiglas block called *buffer*. This buffer was used as support during compression, helping to better distribute stress through the model. The buffer also allowed to establish reference Plexiglas velocities, because of its high incompressibility. The reference velocities served as quality control during acquisition in the models, assuring that there is good coupling between models and transducers. Despite the great reduction in thickness of the rubber discs, the entire experiment was conducted in the linear elastic domain. This is evidenced in Figure 6, which presents the deformation of the inclusions with increasing stress.

RESULTS AND DISCUSSION

Seismograms

The ultrasonic measurements described above led to the P- and S-wave seismograms in Figures 7 and 8 as a function of applied stress. The different P-wave traveltimes are a consequence of the different model dimensions in the y and z directions. We denote the two main polarisations of the S-waves as S_1 and S_2, where the S_1 component is the one with higher velocity. This component is polarised parallelly to the plates, i.e., it can be identified as the S_H wave. Accordingly, the S_2 component is the S_V wave, polarised orthogonally to the plates. Corresponding seismograms were acquired for the model with inclusion.

Velocities

The picked traveltimes (red lines in Figures 7 and 8) together with the model dimensions determine the wave speeds. These velocities will then be used to compute elastic and anisotropic parameters. All velocities were determined in the y direction parallel to the Plexiglas plates and in the z direction perpendicular to the plates. In the z direction, besides crossing the models, the signal also crossed two Plexiglas buffer
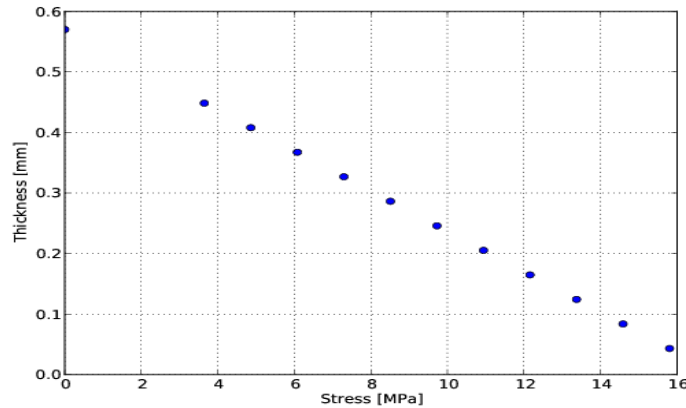
Figure 6: Thickness variation of the inclusions with increasing stress.
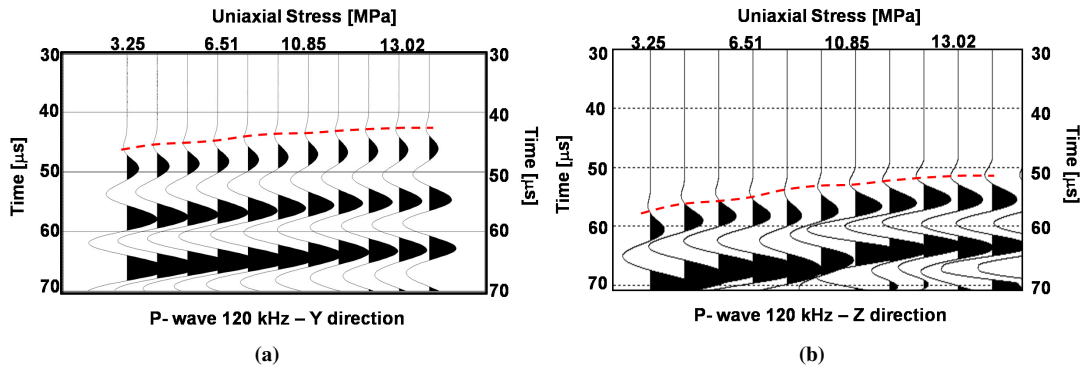

Figure 7: P-wave seismograms acquired for several stress levels in the reference model. Red lines represent first arrivals. (a) Propagation in the y direction. (b) Propagation in the z direction.

blocks. Thus, velocities were calculated according to

$$V_y = \frac{l_y}{t_y - t_d} \quad , \qquad V_z = \frac{l_z - 2l_b}{(t_z - t_d) - 2t_b} \; , \tag{2}$$

where V_j is the (P- or S-wave) velocity of the wave propagating in the j (y or z) direction, t_j and l_j are the traveltime and model dimension in that direction, and t_B and l_b denote the traveltime and size of the buffer. The transducer-induced time delay t_d is a constant of the equipment.

In addition to these directions, similar experiments were carried out under $45°$ with respect to the plates, in order to obtain information about the elastic coefficient C_{12}. Since the measurements were taken in the oblique direction, there is no interference of the buffer. Thus, in this case, velocities were computed according to

$$V_{45} = \frac{l_{45}}{(t_{45} - t_d)/0.88} \tag{3}$$

where V_{45} is the velocity along the model diagonal, and t_{45} and l_{45} are the traveltime and model length in that direction. As before, t_d is the transducer-induced time delay and 0.88 is a correction factor.

All ultrasonic measurements were done under variation of the applied stress. The only difference between the P- and S-wave measurements is the change in the transducers. The P- and S-wave velocities calculated using equations (2) and (3) are shown in Table 1 and Figure 9. Figure 9b only shows three curves because the coupling between transducers and cracked model was not good at the oblique position, giving rise to inconsistencies in the determination of velocities.

We observe that P- and S-wave velocities in both the reference model and the cracked model with inclusions present different regimes of linear variation. For the reference model, a strong variation at low
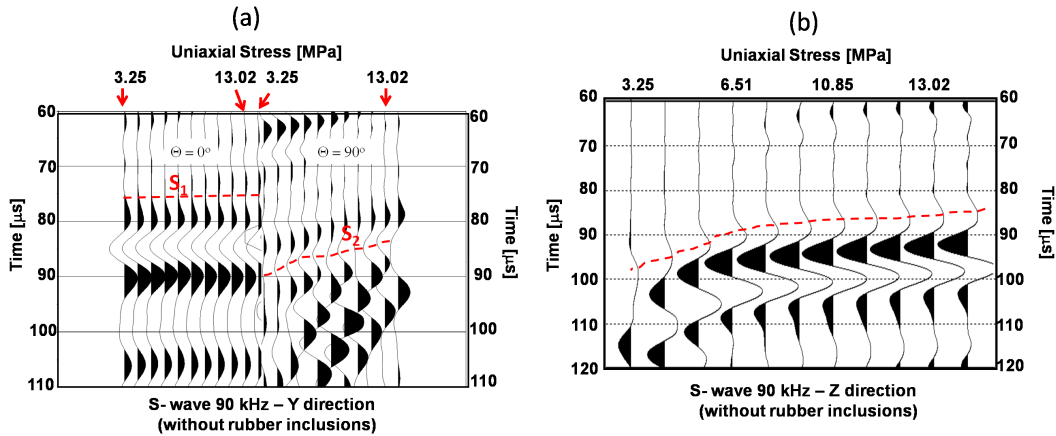
Figure 8: S-wave seismograms acquired for several stress levels in the reference model. Red lines represent first arrivals. (a) Propagation in the y direction with polarisations parallel (left part) and perpendicular to the plates (right part). (b) Propagation in the z direction, where all polarisations produce equivalent arrivals.

Table 1: Velocity data from ultrasonic experiments, values rounded to the nearest integer. See Figure 9.

	Stress [MPa]	3.6	4.8	6.1	7.3	8.5	9.7	10.9	12.2	13.4	14.6	15.8
	$V_P(z)$ [m/s]	1941	2030	2101	2155	2223	2271	2315	2354	2401	2422	2446
	$V_P(y)$ [m/s]	2470	2483	2509	2535	2563	2584	2605	2619	2634	2641	2648
Reference Model	$V_{45°}$ [m/s]	2290	2337	2367	2406	2432	2458	2469	2496	2523	2557	2569
	V_{S1} [m/s]	1241	1241	1241	1241	1241	1241	1241	1241	1241	1241	1241
	V_{S2} [m/s]	1081	1104	1126	1138	1146	1151	1157	1164	1170	1174	1179
	V_{buffer} [m/s]	2683	2683	2683	2683	2683	2683	2683	2683	2683	2683	2683
	$V_P(z)$ [m/s]	1346	1655	1853	1953	2040	2151	2199	2249	2275	2298	NA[†]
	$V_P(y)$ [m/s]	2396	2410	2443	2454	2493	2535	2558	2565	2578	2578	NA
Cracked Model	V_{S1} [m/s]	1257	1257	1257	1257	1257	1257	1257	1257	1257	1257	NA
	V_{S2} [m/s]	1045	1064	1095	1116	1121	1129	1154	1168	1182	1191	NA
	$V_S(z)$ [m/s]	573	634	669	705	747	787	811	900	906	914	NA
	V_{buffer} [m/s]	2683	2683	2683	2683	2683	2683	2683	2683	2683	2683	NA

[†] *Not acquired*

compression (Figure 9) gives place to a weaker variation around 6-7 MPa. In the cracked model, there are three linear regimes, separated at approximately 6-7 and 10-12 MPa. Despite the fact that all velocities increase with increasing stress, the behaviour of the variation is markedly different in the reference model and in the model with inclusions. However, the three linear stress regimes are visible in all parts of Figure 9. A possible interpretation will be indicated below.

Existing rock physics model describe velocities that present a smooth variation as function of stress. Therefore, in the fits below we chose an exponential function of the form

$$V = V_a - Ae^{-k\sigma} \tag{4}$$

to describe the variation, where σ denotes the applied stress. This model also has the advantages of being smooth, asymptotic, and needing few parameters, besides being already implemented in the software used. Moreover, the exponential curves give rise to an asymptotic value V_a which the velocities approach for increasing stress. This can be interpreted as the value for a medium in which the discontinuities vanish. The constant k in the exponent of function (4) can be understood as a kind of stress sensitivity. The higher the factor k in the exponent, the more strongly the velocity depends on stress. It should be noted that V_{S1} is constant throughout the experiment, as can be verified from Table 1 and Figure 9. Thus, there was no need to fit a curve to the data.
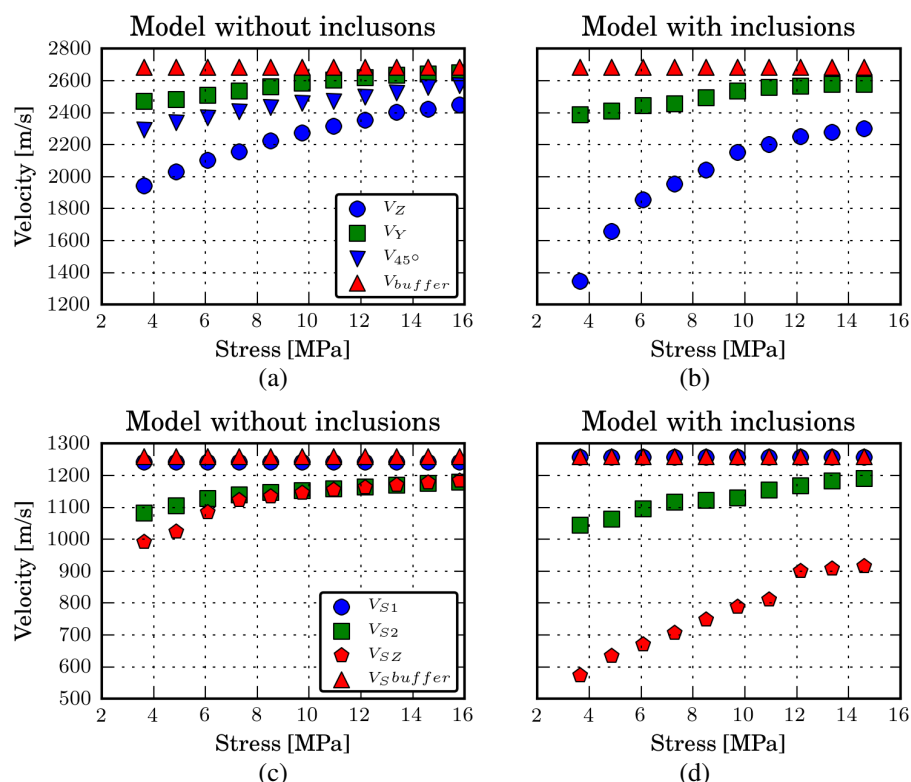
Figure 9: P- and S-wave velocities measured with transducers of central frequencies 120 kHz and 90 kHz, respectively. (a) P-wave velocities in the reference model; (b) P-wave velocities in the model with inclusions; (c) S-wave velocities in the reference model; (d) S-wave velocities in the model with inclusions.

Table 2: Fitting parameters for exponential P-wave velocity fit. See Equation 4 for meaning of the terms.

	Reference Model					Cracked Model		
	$V_P(y)$	$V_P(z)$	$V_{S2}(y)$	$V_S(z)$	$V_P(y)$	$V_P(z)$	$V_{S2}(y)$	$V_S(z)$
V_a	2770	2664	1185	1188	2716	2348	1320	1609
A	416	1039	212	528	473	2563	351	1189
k	0.08	0.10	0.20	0.30	0.09	0.30	0.07	0.04

Figures 10 and 11 show the exponential fit of the wave velocities in the horizontal and vertical directions. In both cases, the fit is quite good, with rather small residuals distributed randomly around the fitted curve. From the parameters of the exponential fit (see Table 2), we see that the P velocity in the horizontal direction is less sensitive to stress increase than in the vertical direction. The P velocity measured in the oblique direction exhibits an intermediate behaviour.

In the fitted function for the vertical P velocity in the reference model, the saturation (asymptotic) value V_a is quite close to the velocity measured in the buffer (2664 m/s *vs* 2683 m/s), with a difference of less than 1%. The residual values for the fit are of the order of errors expected from the experiment.

The vertical P velocity in the model with inclusions is not as well fitted by an exponential function of the type (4) as in the reference model, as can be seen in Figure 11. Up to 9 MPa the fit gives residuals of about 30 m/s, while from this stress level upwards, the residuals fall below 5 m/s, within the error margins from the experiment. The corresponding fitting curves for the S waves are shown in Figures 12 and 13. The fitting parameters are also contained in Table 2. With few exceptions, the residuals are of the expected size for all S-wave fits.
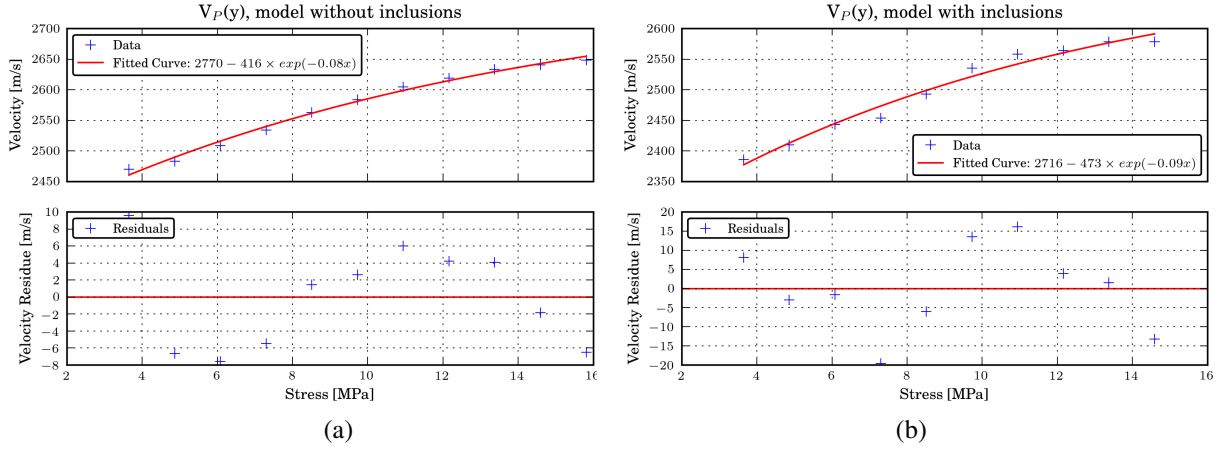
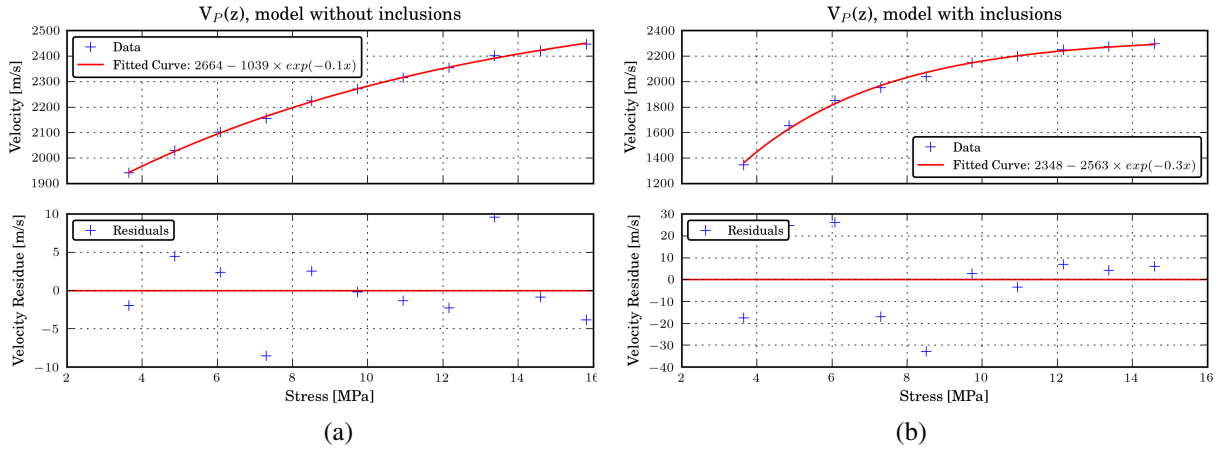**Figure 10:** Exponential fit for V_P in the y direction. (a) Reference model; (b) cracked model.

Figure 11: Exponential fit for V_P in the z direction. (a) Reference model; (b) cracked model.

Geometrical characteristics of the Inclusions

The geometrical characterization of discontinuities, fractures inclusive, is perhaps the most valuable product that could be derived from the seismic data. The geometrical character of the fractures plays an important role in the definition of fluid flow, thus being highly relevant in the production of fractured reservoirs. In this subsection we will investigate the relationship between the geometrical characteristics of the inclusions and the applied stress. The observed geometrical characteristics are summarized in Table 3.

Crack diameter. Specifically, we study the diameter variation as function of the longitudinal deformation with the increasing stress (see Figure 14). Our analysis is a variation from that of Olson (2003), who has studied vein and dyke lengths as function of their width. There are two possible interpretations of the data in Figure 14. Clearly this function can be interpreted as being composed of three linear regimes (see Figure 14a), separated at the same stress levels mentioned in connection with Figure 9. The fit residuals for the three curves are $0.028; 1.2 \times 10^{-33}$ and 0.0012 respectively for the blue, red and green lines.

An alternative is an exponential fit, as shown in the Figure 14b. In this case, the data were fitted via an exponential function:

$$d = d_a - A_d e^{-\beta h} \quad , \tag{5}$$

where h denotes the deformation and d the crack diameter. The fitting parameters and standard deviations are $d_a = 10.372061 \pm 0.037405$, $A_d = 2.866622 \pm 0.0943954$, and $\beta = 5.565112 \pm 0.357925$. In other words, equation (5) describes a saturation curve that asymptotically approaches the maximum diameter of
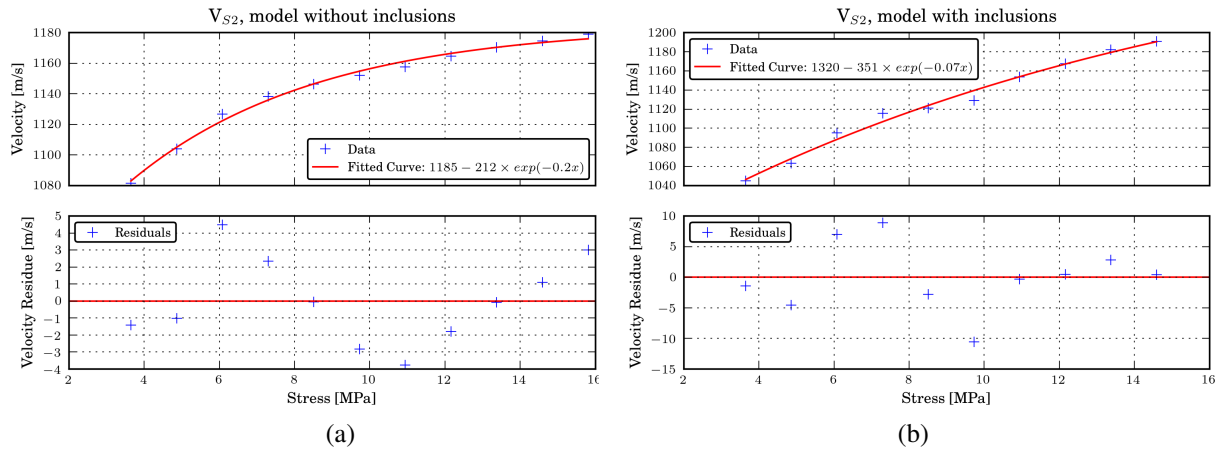
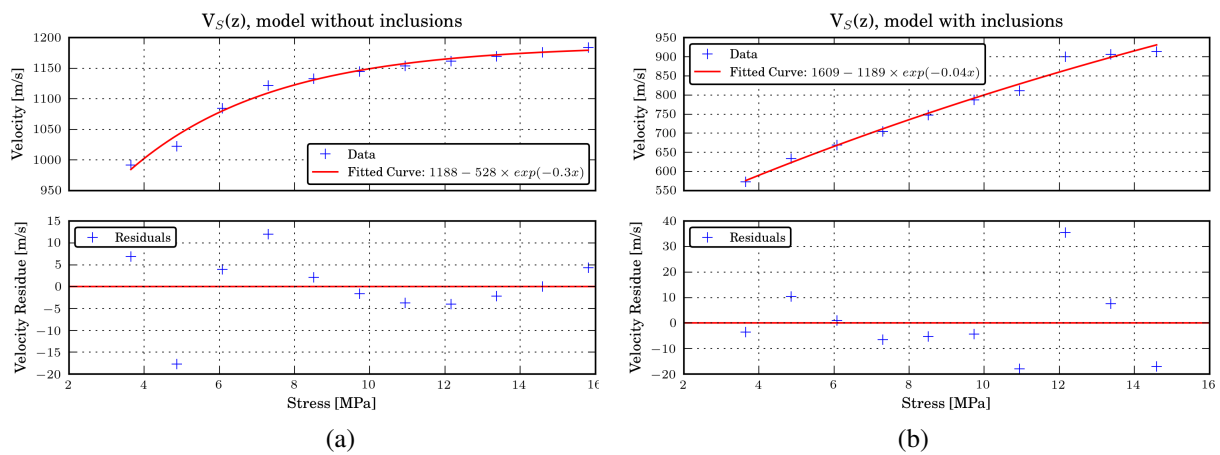**Figure 12:** Exponential fit for V_{S2} in the y direction. (a) Reference model; (b) cracked model.

Figure 13: Exponential fit for V_S in the z direction. (a) Reference model; (b) cracked model.
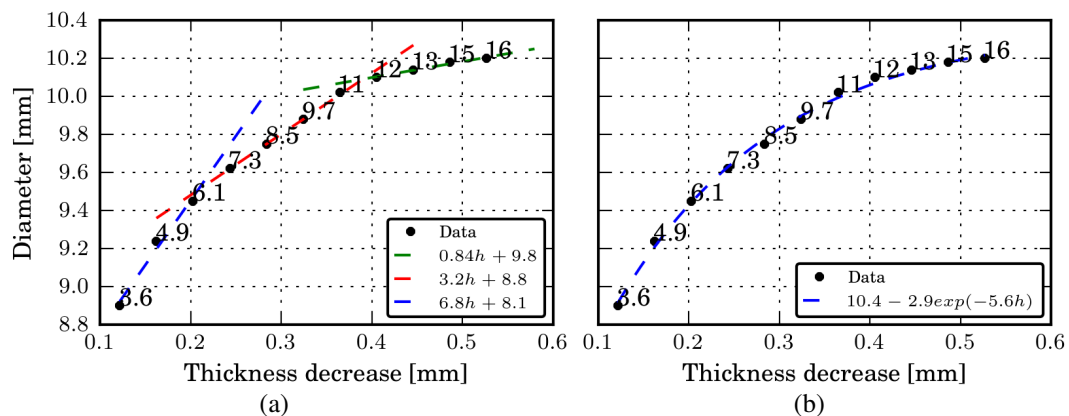

Figure 14: Inclusion thickness versus diameter during the experiment. Black numbers are the applied stress, in MPa. (a) Interpretation with three linear segments. (b) Exponential fit.

the inclusions of 10.4 mm. A more detailed analysis of the exponential fit and its residual is shown in Figure 15. We observe that the residuals are smaller than the measurement error.

Note that the excellent exponential fit indicates that our compression of soft rubber inclusions still might be correctly described by fracture mechanics principles (Gross and Seelig, 2006). Of course, our results

Table 3: Stress effects over inclusion dimensions. These data are also shown in Figures 14 and 16.

Stress [MPa]	0.0	3.6	4.8	6.1	7.3	8.5	9.7	10.9	12.2	13.4	14.6	15.8
Diameter [mm]	3.83	8.90	9.24	9.45	9.62	9.75	9.88	10.02	10.10	10.14	10.18	10.20
Thickness [mm]	0.57	0.45	0.41	0.37	0.33	0.29	0.25	0.21	0.16	0.12	0.08	0.04
Deformation [mm]	0.00	0.12	0.16	0.20	0.24	0.28	0.32	0.36	0.41	0.45	0.49	0.53
Aspect Ratio[‡]		0.14	0.050	0.044	0.039	0.034	0.029	0.025	0.021	0.016	0.012	0.008	0.004
Fracture density[‡]	0.061	0.059	0.055	0.050	0.045	0.038	0.032	0.025	0.017	0.009	NA[†]	NA

[‡] *dimensionless*   [†] *Not acquired*
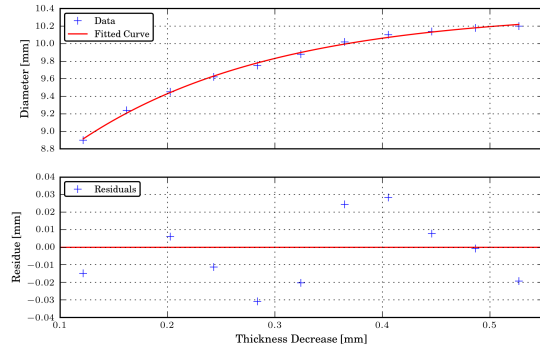
Figure 15: Exponential fit and residuals, following the method of Olson (2003). Magnitude of residuals is less than the linear measurement error.
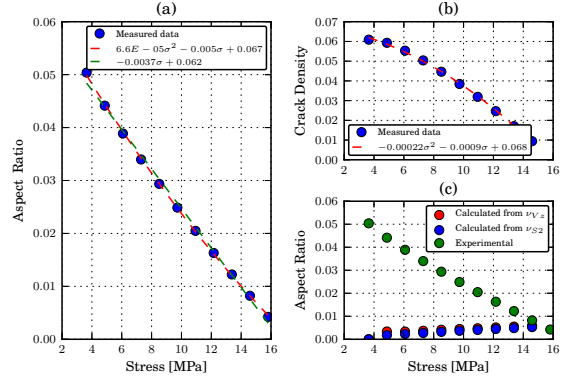
Figure 16: Fracture parameters as function of applied uniaxial stress. (a) Fit of aspect ratio; (b) fit of crack density; (c) aspect ratio compared to theoretical prediction.

for the fitting parameters differ from those of Olson (2003), which probably means that these parameters are material constants. Still, the differences in diameter and width of fractures between our experiments and the field data of Olson (2003) are rather small. Further experiments will be necessary to investigate if other materials will better preserve scalability as crack filling material in this sense.

Aspect ratio. We also calculated the aspect ratio r_a for an equivalent medium, based on the parameters of the model with inclusions. The calculated data are shown in Figure 16. In the experiment, the system was open to atmosphere and therefore, we considered pore pressure to be zero. The aspect ratio shows an almost linear dependence on stress (see Figure 16a).

In Figure 16c, we compare these data to the theoretical prediction obtained by inverting the equation of Mavko (2009, p. 66). It states that the necessary stress to achieve crack closure is related to the aspect ratio by

$$\sigma_c = \frac{1}{2(1 - \nu^2)} r_a E \ , \tag{6}$$

where σ_c is the crack closure stress, ν is the Poisson ratio, r_a the aspect ratio and E is Young's modulus. Taking $E = 2\mu(1 + \nu)$, where μ is the shear modulus, and rearranging, we find

$$r_a = \left(\frac{1 - \nu}{\mu} \right) \sigma_c \ . \tag{7}$$

This result resembles the corresponding equation of Verdon et al. (2008), with the exception of a factor $2/\pi$ and an initial state aspect ratio r_a^0. The expression given by those authors reads

$$r_a = r_a^0 - \frac{2(1 - \nu)}{\pi\mu} \sigma_c \tag{8}$$

At this point, we do not have enough data to decide which of these formulas is better. To clarify this point, other detailed studies are necessary. However, we can state that in the experiment, the crack closure
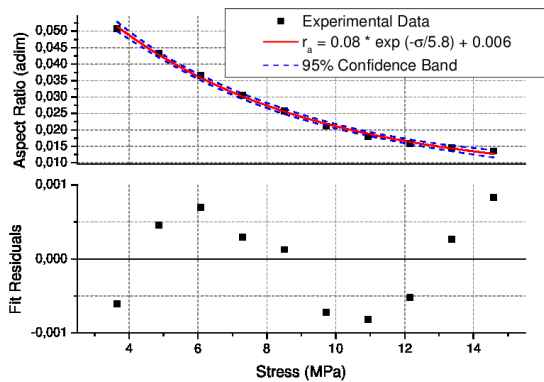
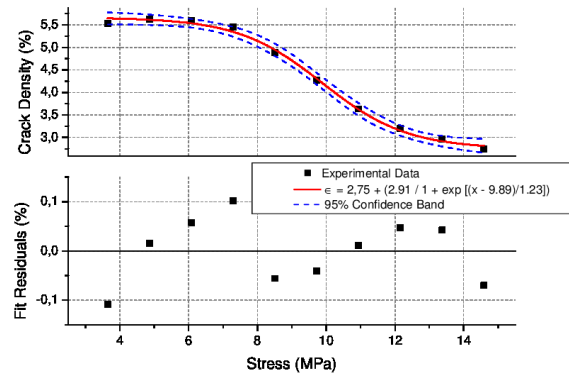**Figure 17:** Curve fit for aspect ratio. Blue lines are the 95% confidence interval..

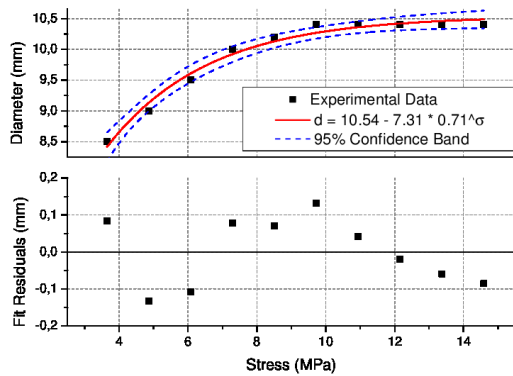**Figure 18:** Sigmoidal function fit for fracture density. Blue lines are the 95% confidence interval.

Figure 19: Exponential function fit for inclusion diameter. Blue lines are the 95% confidence interval.
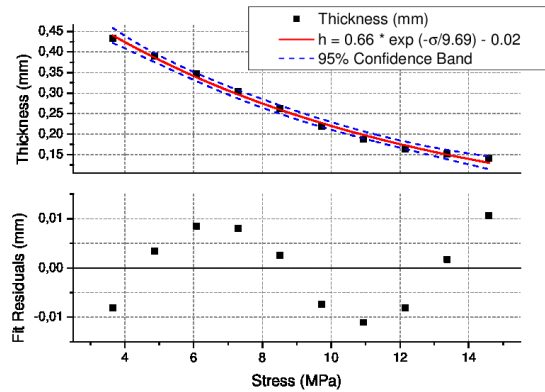

Figure 20: Exponential fit for inclusion thickness. Blue lines are the 95% confidence interval.

stress σ_c was not attained. Thus, we understand that it is incorrect to use any of the preceding relations to characterize the crack aspect ratio before closure, at least without taking into account that ν and μ also vary with stress.

We also studied other fits to the experimental data with regards to the rubber inclusions, based on the principles outlined in the Velocities subsection. The graphs are presented in Figures 17 to 20. The aspect ratio as a function of stress is well-fitted by an exponential-decay function, whose parameters are shown with the fitted curve in Figure 17. The first term can be understood as the initial aspect ratio, while the last one can be seen as the aspect ratio at closure.

The crack density as a function of stress is well-fitted by a sigmoidal type curve, as shown in Figure 18. In this case, the stress values of 6-7 MPa and 11-12 MPa, which define the three different linear regimes for the velocity, also represent the transition between the parts of the sigmoidal function. These limits can be interpreted as being the transitions between permeability regimes of the model, as discussed below.

The inclusion diameter is well described by an exponential saturation curve (see Figure 19). In this case, the (constant) saturation value represents the inclusion's maximum diameter under infinite compression.

Finally, the graph shown in Figure 20 displays the asymptotic decay of thickness as function of increasing stress, fitted by an exponential curve. The first term represents the original inclusion thickness. The error of about 0.1 mm is of the order of the expected experimental error. The last constant represents the asymptote, i.e., the minimum thickness that would be reached under infinite stress.
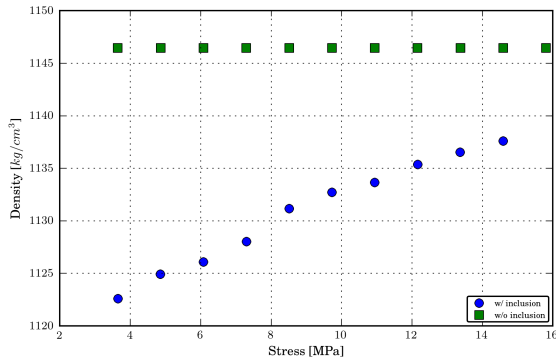
Figure 21: Calculated density for the reference model (squares) and cracked model (circles).
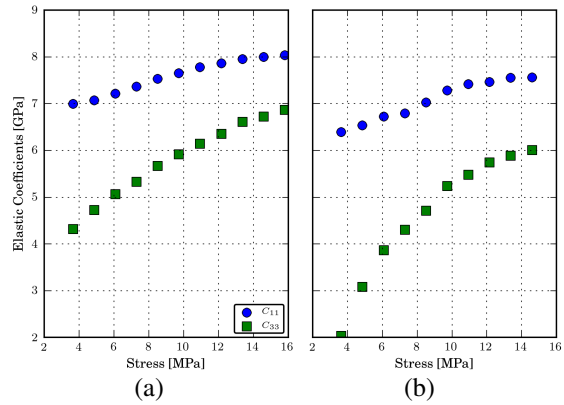

Figure 22: Elastic coefficients C_{11} and C_{33}. (a) Reference model; (b) cracked model.
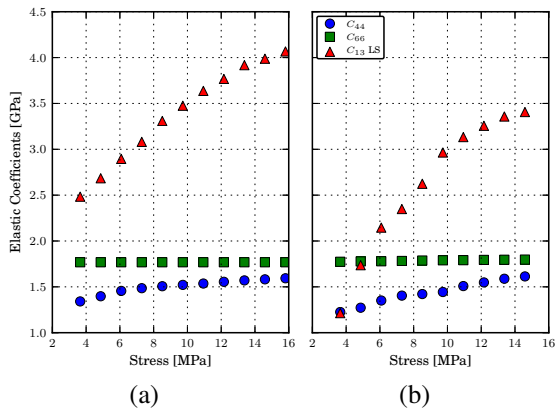

Figure 23: Elastic parameters C_{44} and C_{66} as well as an approximation to C_{13} obtained by the Linear Slip Displacement of Schoenberg (1980). (a) Reference model; (b) cracked model.
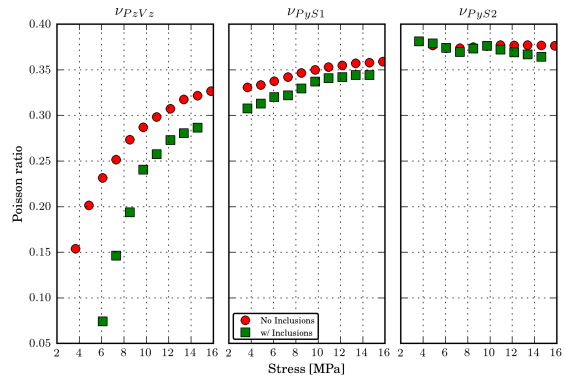

Figure 24: V_P/V_S ratios, measured in different directions, for the reference model (circles) and the model with inclusions (squares).

Elastic Coefficients

Next we determined the elastic coefficients, which rule the seismic behaviour of materials under stress. Figure 21 shows the density of the models under stress, and Figure 22 depicts the coefficients C_{11} and C_{33} calculated from the velocities determined earlier.

The density in the reference model is approximately constant, while it increases with stress in the cracked model, due to compression of the rubbers discs, as expected (Figure 21). The behaviour of the elastic coefficients seems to mimic that of the velocities (Figure 22). In the cracked model, both components C_{11} and C_{33} show slope variations at the same stress levels around 6-7 and 10-12 MPa, indicating and reinforcing our interpretation (see below). Both components C_{11} and C_{33} exhibit a smoother behaviour in the reference model than in the model with inclusions.

As a next step, we calculated the elastic parameters C_{44}, C_{66}, and, using the Linear Slip Displacement approximation (Schoenberg, 1980), C_{13}. Figure 23 shows C_{66} to be insensitive to stress increase and to the presence of inclusions. The shear modulus $\mu = C_{44}$ in both models increases with stress. As expected the soft rubber inclusions lower the overall shear modulus in the cracked model. In the reference model, the shear modulus seems close to reaching a saturation level, while in the cracked model, such a saturation cannot be found. In the cracked model, the Lamé parameters also seem to exhibit the three linear regimes that we observed in the velocity data (Figure 9), aspect ratio (Figure 14) and elastic coefficients (Figure 22). These observations are coherent with the notion that S-waves are less sensitive to anisotropy than P-waves, since the S-wave velocities depend on different elastic parameters.
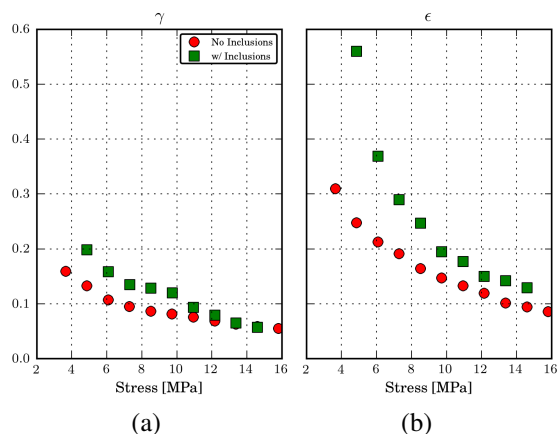
Figure 25: Thomsen's parameters, calculated for the reference model (circles) and the model with inclusions (squares). (a) γ; (b) ϵ.
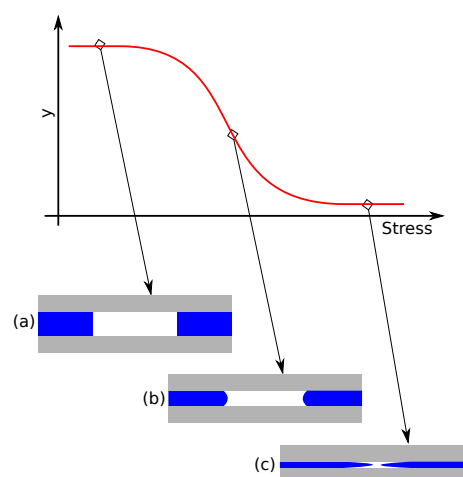
Figure 26: Interpretation. (a) Inclusions with small deformation; (b) deformation increases; (c) no more air can be expelled from the model.

The V_P/V_S ratio in the vertical direction shows a strong initial increase that diminishes with increasing stress (see Figure 24). In the horizontal direction, the V_P/V_{S1} ratio exhibits much smaller variations, and the V_P/V_{S2} ration remains approximately constant. There is some difference between the curves for the reference model and for that on the model with inclusions, with smaller V_P/V_S ratios for the model with inclusions than for the reference model. As before, also these curves can be interpreted as consisting of three linear regimes.

Thomsen's γ and ϵ present a marked decrease, both for the reference model and the model with inclusions, suggesting that there might be an asymptote beyond 16 MPa. For γ, the model with inclusions shows a yet faster decrease that in the reference model. A Similar observation was made with regards to ϵ, however, there is some separation between the results from the reference model and the model with inclusions. The graph for Thomsen's parameter as functions of applied stress is shown on Figure 25.

Interpretation

Figure 26 shows our interpretation model for the linear regimes in the elastic and anisotropic parameters as functions of stress. In the first regime, indicated by inset (a), the inclusions are in an almost undeformed state. The inter-inclusion space is filled with air and the system is open to atmosphere. Upon increased stress, air is expelled from the sample. At the beginning of the second regime, at 6-7 MPa, the plates start to touch between the inclusions (inset b). At this stage, the inclusions are already deformed and the inter-inclusion space is already reduced. We infer that effective-medium behaviour starts at this stage. At about 10-12 MPa begins the third regime, in which no further air can be expelled, as all spaces are almost closed (inset c) and no longer communicating. Further modifications result from compaction of the plates and rubber inclusions, though still within the limits of elasticity. In the reference model, since there are no inclusions, the air would have been expelled much earlier, at about 6-7 MPa, and no further slope variations should be expected. This coincides with the observations.

CONCLUSIONS

We carried out ultrasonic P- and S-wave measurements over two physical models. The reference model was built by stacking 55, 1.5 mm thick Plexiglas plates and the model with inclusions added 30 neoprene disks with diameter 3.6 mm and thickness 0.57 mm between each pair of the same plates. Under variation of applied stress, we acquired ultrasonic P- and S-wave seismograms for different propagation directions. From the model parameters and first-arrival traveltimes, we calculated seismic velocities and overall elastic medium parameters. Even though the maximum stress attained in this experiment is low in comparison

to actual reservoir stress levels, our results indicate that the experiment was able to sample most of the variation in the properties of the materials employed in the models.

The P- and S-wave velocities show different variation patterns in the reference model and in the model with inclusions. The general tendency of the velocities is to increase with increasing stress. In the reference model, a strong variation at the start of compression changes into a smaller variation upwards from 6-7 MPa. In the model containing penny shaped neoprene inclusions, there are three separate linear regimes, limited at around 6-7 MPa and 10-12 MPa. Since the experiment was conducted in discrete stress steps, the stresses where the transitions occur cannot be determined with higher precision. The three linear regimes can be interpreted as regimes of different closure of the spaces between the inclusions.

In an alternative interpretation, we also found good exponential fits for the velocities for both models, with residuals within 1% of the determined velocities and for the most cases, within the expected range of experimental error. In the reference model, the P velocity given by the asymptote of the adjusted exponential function is close to the one measured in the Plexiglas buffer.

Verdon et al. (2008), who worked with core samples taken from different depths along a well, observed a similar velocity behaviour as a function of stress. The samples had differing degrees of damage, related to the difference between their original stress state and laboratory conditions under which they were prepared. Since our experiment uses different materials, our results do not reproduce exactly those from Olson (2003) or (Verdon et al., 2008), but seem to rely on the same fracture mechanics principles (Gross and Seelig, 2006).

In the same sense, the variation in fracture length and aperture we achieved in the experiment is small when compared with field data. We believe that our model could capture the effects of a mechanism that is also applicable to reservoir rocks, where the mechanism can be understood as the generation of unloading fractures in rock cores and lateral samples, when brought to surface. The observed behaviour in the model presents a high similitude to published data.

Due the experiment setup and choice of materials, it was only possible to reproduce a range of value of stresses, fracture densities, and aspect ratios that we believe to be small compared to those that occur in hydrocarbon reservoirs. Another source of discrepancies between our data and published data is the fact that our fractures were actually inclusions of soft material, without pore pressure that impacts the behaviour of rocks under high stresses. Despite those differences, we feel that the data we presented are representative of the behaviour of rocks under low to medium stresses.

The three different regimes were also observable for the elastic parameters C_{ij}, and for some of the geometrical parameters of the models. reinforcing our interpretation of the air being forced out of the model and the formation of an effective medium behaviour. The parameter C_{66} is insensitive to stress increase and to the presence of neoprene inclusions, since the Plexiglas plates are much more rigid than the rubber. The shear modulus $\mu = C_{44}$ in the model with inclusions presents lower values than in the reference model, and rises quickly with stress. The soft rubber inclusions lower the overall rigidity of the models, as one would expect from mixing laws.

The V_P/V_S ratios calculated in the different propagation directions also allow to interpret the three different regimes. The V_P/V_S ratio in the model with inclusions is always lower that that for the reference model, indicating that the P velocity is stronger affected by the inclusions than the S velocity. The horizontal V_P/V_S ratios are less affected by the increasing stress than the vertical ones, with the one from the S2 polarisation being practically constant.

In summary, the availability of velocities measured for different polarisations in different propagation directions allows to determine the elastic coefficients of the medium. From these coefficients, it is possible to characterize the medium. On the basis of corresponding detailed information from rock samples or analogous models, or even cross-well data, it might be possible to characterize the properties of a fractured reservoir or even figure out which regions of a reservoir are more extensively fractured.

REFERENCES

Aguilera, R. (1998). Geologic aspects of naturally fractured reservoirs. *The Leading Edge*, 17(12):1667.

Crampin, S. (1981). A review of wave motion in anisotropic and cracked elastic-media. *Wave Motion*, 3(4):343–391.

Crampin, S. (1984a). Effective anisotropic elastic constants for wave propagation through cracked solids. *Geophysical Journal-Royal Astronomical Society*, 76(1):135–145.

Crampin, S. (1984b). An introduction to wave propagation in anisotropic media. *Geophysical Journal of the Royal Astronomical Society*, 76(1):17–28.

Figueiredo, J. J. S. (2012). *Modelagem física de meios fraturados anisotrópicos e estudo da birrefringência sísmica em função dos parâmetros anisotrópicos*. PhD thesis, Universidade Estadual de Campinas, Campinas, Brazil.

Figueiredo, J. J. S., Dyaur, N., Omoboya, B., Wiley, R., William, A., Schleicher, J., and Stewart, R. A. (2011a). Influence of source frequency on shear wave splitting - an experimental approach. In *73rd EAGE Conference and Exhibition*, pages 1–5, Vienna, Austria.

Figueiredo, J. J. S., Stewart, R. R., Dyaur, N., Schleicher, J., Omoboya, B., Wiley, R., and William, A. (2011b). Frequency dependence of elastic and attenuation properties of cracked media: Ultrasonic modeling studied. In *12th International Congress of the Brazilian Geophysical Society*, Rio de Janeiro, Brazil.

Figueiredo, J. J. S., Stewart, R. R., Schleicher, J., Dyaur, N., Omoboya, B., Wiley, R., and William, A. (2012a). Shear-wave anisotropy from aligned inclusions: Ultrasonic frequency and attenuation properties. *Geophysical Journal International*, submitted.

Figueiredo, J. J. S. d., Schleicher, J., Stewart, R. R., and Dyaur, N. (2012b). Estimating fracture orientation from elastic-wave propagation: An ultrasonic experimental approach. *Journal of Geophysical Research*, 117(B8):B08304.

Gross, D. and Seelig, T. (2006). *Fracture Mechanics*. Mechanical Engineering Series. Springer.

Hudson, J. A. (1981). Wave speeds and attenuation of elastic waves in material containing cracks. *Geophysical Journal of the Royal Astronomical Society*, 64(1):133–150.

Krey, T. and Helbig, K. (1956). A theorem concerning anisotropy of stratified media and its significance for reflection seismics. *Geophysical Prospecting*, 4(3):294–302.

Marcondes, P. E. P., Figueiredo, J., Schleicher, J., Dyaur, N., and Stewart, R. R. (2012a). Lithostatic stress driving changes on fracture aspect ratio - ultrasonic experiment and results. In *EAGE Conference and Exhibition*, Copenhaguen, Denmark.

Marcondes, P. E. P., Figueiredo, J. J. S., Eftekharifar, M., Schleicher, J., Dyaur, N., and Stewart, R. R. (2012b). Experimental relations between stress and fracture properties on synthetic anisotropic media. In *SEG Annual Meeting Expanded Abstracts*, Las Vegas, USA. SEG.

Mavko, G., Mukerji, T., and Dvorkin, J. (2009). *The Rock Physics Handbook*. Cambridge University Press, second edition edition.

Nelson, R. A. (2001). *Geologic Analysis of Naturally Fractured Reservoirs*. Gulf Professional Publishing, 2 edition.

Olson, J. E. (2003). Sublinear scaling of fracture aperture versus length: An exception or the rule? *Journal of Geophysical Research*, 108(B9):2413.

Omoboya, B., de Figueiredo, J. J. S., Dyaur, N., and Stewart, R. R. (2011). Uniaxial stress and ultrasonic anisotropy in a layered orthorhombic medium. In *SEG Technical Program Expanded Abstracts*, volume 30, pages 2145–2149, San Antonio, USA.

Schoenberg, M. (1980). Elastic wave behavior across linear slip interfaces. *The Journal of the Acoustical Society of America*, 68(5):1516.

Schoenberg, M. and Sayers, C. M. (1995). Seismic anisotropy of fractured rock. *Geophysics*, 60(1):204–211.

Tsvankin, I. (2005). *Seismic Signatures and Analysis of Reflection Data in Anisotropic Media*. Gulf Professional Publishing.

Verdon, J. P., Angus, D. A., Michael Kendall, J., and Hall, S. A. (2008). The effect of microstructure and nonlinear stress on anisotropic seismic velocities. *Geophysics*, 73(4):D41.

STRUCTURE ENHANCING FILTERING WITH THE STRUCTURE TENSOR

R. Morelatto and R. Biloti

email: *rodrigo.geof@gmail.com, biloti@ime.unicamp.br*

keywords: *Structure tensor, Slopes, Plane-wave destructor, Structure prediction*

ABSTRACT

The structure tensor is a very versatile tool. It can be used to detect edges, estimate coherency and local slopes. In this work we employ the structure tensor to estimate local slopes. We compare the slopes obtained with this tool with the slopes obtained by two different implementations of plane-wave destruction filters. Those three methods were tested against three different datasets, two synthetic and one real. The slopes detected through the structure tensor were reliable and comparable to the ones obtained with plane-wave destruction filters. Finally, we present an application for the slopes detected by the structure tensor. We show how to employ them to filter seismic data along structures.

INTRODUCTION

Determining local slopes is of great interest in seismic data analysis. They can be used to accomplish many of time-domain imaging tasks, like normal moveout and prestack time migration (Ottolini, 1983; Fomel, 2007c). Local slopes can also be used to interpolate data and filter along seismic structures (Fomel, 2002; Liu et al., 2010). In this work we compare the local slopes obtained via the well established method of plane-wave destruction (Claerbout, 1992) to the ones obtained using the structure tensor (Bakker, 2002).

The structure tensor was applied to seismic data analysis and filtering many times before. Bakker (2002) gives a very comprehensive description of the applications of structure tensors to seismic data filtering. They can also be used to identify and create clusters of areas of interest in seismic data (Faraklioti and Petrou, 2005) and to edge preserving smoothing by diffusion filtering of seismic data (Hale, 2009; Lavialle et al., 2007).

As noted by Bakker (2002), the amount of data to interpret has grown faster than the number of capable interpreters. Also, there are more pressure for quicker interpretation results, since risk management decisions are taken based on them. One way to ease the burden imposed on interpreters and to make automatic interpretation more reliable is to use structure oriented filtering. This procedure reduces noise and enhances reflector continuity. It also removes some subtle geological features, resulting in seismic sections easier to interpret.

Driven by those motivations, Fehmers and Höcker (2003) have proposed to use the structure tensor to perform structure oriented filtering by anisotropic diffusion. This procedure results in structure simplification and make the interpretation process more agile. Bakker (2002) also tried to address that problem by using orientation adaptive filtering and edge preserving filtering with the structure tensor. His work also features the use of the structure tensor to detect faults. In this paper we propose to study a third approach, by using structure prediction filtering (Liu et al., 2010). While Liu et al. (2010) advocate the use of plane-wave destruction to estimate dips, we propose to employ the dips detected by the structure tensor.